materials

MDPI

Article

Enhanced visible-light active WO_3 thin films towards air purification: effect of the synthesis conditions

Anna Pancielejko [1], Marta Rzepnikowska [2], Adriana Zaleska-Medynska [2], Justyna Łuczak [1], Paweł Mazierski [2*]

[1] Department of Engineering Process and Chemical Technology, Faculty of Chemistry, Gdansk University of Technology, 80-233 Gdansk, Poland; anna.pancielejko@pg.edu.pl (A.P.); justyna.luczak@pg.gda.pl (J.Ł.)
[2] Department of Environmental Technology, Faculty of Chemistry, University of Gdansk, 80-308 Gdansk, Poland; marrzepn21@gmail.com (M.R.); adriana.zaleska-medynska@ug.edu.pl (A.Z.-M.)
* pawel.mazierski@ug.edu.pl (P.M.); Tel.: +48-58-523-52-30

Received: date; Accepted: date; Published: date

Abstract: Taking into consideration, our current environmental situation in the world people should face with growing problem of air and water pollution. Heterogeneous photocatalysis is highly promising tool to improve both, air and water quality through decomposition/mineralization of contaminations directly into harmless CO_2 and H_2O under ambient conditions. In this contribution we focused on the synthesis of self-assembly WO_3 thin films *via* an electrochemical approach in the aqueous electrolyte containing fluoride ions towards air purifications. The effect of preparation conditions such as applied potential (10 – 50 V), anodization time (15 – 120 minutes), concentration of H_2SO_4 (0.5 – 1.5 M) and NaF (0.1 – 1.0 wt.%) on the morphology, photocurrent response and photocatalytic activity addressed to removal of air pollutant in the presence of as-prepared WO_3 samples were thoroughly examined and presented. The results revealed the growth of nanoplatelets and their gradual transformation into flower-like structure. The oxide layers and platelets thickness of the WO_3 samples were found to be proportionally related with the synthesis conditions. The photocatalytic ability towards air purification was evaluated by degradation of toluene from air mixture using low-powered LEDs as an irradiation source (λ_{max} = 415 nm). The highest photoactivity was achieved in presence of the sample which possessed well-ordered, regular shape and repeatable distribution of flower buds (100% of degradation). The results have confirmed that the oxide layer thickness of the anodic WO_3 significantly affected the photocatalytic activity, which increased with the increasing thickness of WO_3 (to 1.05 μm) and then had a down trend. The photocurrent response evidenced that well-organized sample had the highest ability in photocurrent generation under UV-Vis and Vis irradiation. Finally, a possible growth mechanism of WO_3 NFs was also discussed.

Keywords: WO_3 nanoflowers; electrochemical anodization; toluene degradation; visible light induced photocatalysis;

1. Introduction

Air pollutions are the major cause of global environmental threats. They contribute to the formation of respiratory diseases, infectious diseases, acute toxic effects, cancers as well as reproductive disorders and allergies. The World Health Organization reports that every year over 4.2 million deaths is a result of exposure to ambient air pollutant[1]. Moreover, air pollutants adversely affect the world, disrupting photosynthesis, transpiration and respiration. Secondarily, they contaminate water and soil. They increase the acidity of drinking water as well as content of heavy metals such as lead, copper, zinc or cadmium in the water. Acidified water destroys plumbing installations, washing away various toxic substances from it. They cause corrosion of metals and building materials. Air pollutants have also negative impact on climate change. The main problem which needs to be solved today it is a successful decomposition/mineralization of air contamination. Therefore, an innovative and effective method of removing harmful substances from environmental are sought.

Advanced oxidation processes (AOPs) have been extensively studied to reduce a great variety of pollutants present in various environmental media[2–4]. Among them, special attention has been paid for the application of heterogeneous photocatalysis in environmental applications for the remediation of polluted air and water. The photocatalytic effects exerted by redox reaction are caused by photoinduced of electrons (e^-) from the valence band to the conduction band leaving positive holes (h^+) behind in very short time (femtoseconds) under the influence of UV-Vis irradiation. Several reactive species, including formation of the high reactive hydroxyl radicals (•OH) and superoxide radicals ($O_2^{\bullet-}$), are generated through reaction of e^- and h^+ which are considered to be involved in the oxidative and reductive reactions in photocatalysis. The generated reactive oxygen species react with adsorbed gas and/or water pollutants leading to the degradation/mineralization them into CO_2 and H_2O[5,6]. Successful photocatalytic air purification relies on the following parameters: *(i)* photon absorption of semiconductor photocatalysts and *(ii)* surface properties of photocatalysts, in particular, keeping clean photocatalyst surface free from the accumulation of recalcitrant intermediates and products during the processes[7,8].

Currently, the most studied photocatalyst which holds a great potential as very effective photoinduced photocatalyst is frequently used to decompose organic and inorganic contaminations from water and air due to its good chemical stability, high oxidizability, non-toxicity and low-cost preparation of nano- and microparticles is titanium dioxide (TiO_2). However, the main drawback of it is wide band gap (3.2 eV for anatase) and consequently only small fraction of the solar irradiation can be absorbed by this material (~4%)[9,10]. Many studies reported that sufficient doping of cations or anions into TiO_2 layers to create certain states within the band gap energy may led to achieved visible light driven TiO_2 photocatalysts[11]. However, those modification have a number of fails, such as its thermal instability and formation of recombination centres for photoinduced charge carriers, which significantly decrease its photocatalytic ability[12]. Therefore, designing and/or further development of an efficient visible light active photocatalyst is particularly critical need for air purification.

From a practical point of view, tungsten trioxide (WO_3) became an alternative photocatalytic material with interesting optical, electrical and structural properties [13]. In terms of chemical stability and inertness, WO_3 exhibits the same attributes as TiO_2. In addition, it possess a lower band gap energy level (between 2.4 and 2.8 eV), stable physicochemical properties and strong resilience to photocorrosion effects[10,14]. Furthermore, it has been considered a great interest due to ability to *(i)* decontaminate polluted water[15,16], *(ii)* detect hazardous gases[17–19] and *(iii)* solar energy conversion[20,21].

Numerous studies reported different synthesis approach of WO_3 nanostructures including sol-gel technique[22–24] electrochemical deposition[25], chemical vapour deposition[26,27], electrochemical oxidation[28,29], magnetron sputtering[30–32], ion-beam evaporation[33,34] and atomic layer deposition[35] have been described. Among them, an anodization technique attracts considerable attention due to low cost and simplicity of a synthesis route. Furthermore, the possibility of controlling and adjusting a growth process by tuning anodization parameters (such as applied potential, synthesis time and temperature) as well as electrolyte composition makes this technique more interesting for fabricating metal oxide nanostructures with controllable pore size, good uniformity, and conformability over large areas[36–38]. However, several studies have reported that it is still a challenge to obtain well-aligned and uniformity of anodic WO_3 nanostructures instead of nanoporous[13,39–41]. First mention about preparation of porous WO_3 using galvanostatic anodization of W foil in oxalic acid electrolyte, was described by Grimes *et al.*[42]. It was found that the obtained nanoporous tungsten oxide exhibited more regular surface with smaller pore size in compare with results described previously for other methods. Self-organized nanoporous structure by anodizing W foil in electrolyte composed of 1 M sulphate acid and 0.5 wt.% sodium fluoride was reported by Schmuki *et al.*[37]. The ability to control the synthesis conditions allowed them to obtain desired self-ordered oxide structure exhibiting higher photocurrent efficiency than a compact oxide layer. Sadek *et al.* described the growth process of WO_3 nanoplatelets during the anodization of tungsten foil in a nitric acid environment at higher temperatures[43]. The combination of the

synthesis parameters with high temperature led the authors to obtained relatively thick films of nanoplatelets with potential application in photosensitive devices. Flower-shaped tungsten oxide nanostructure prepared in an acidified electrolyte solution containing fluoride ions was reported by Amal *et al.*[29,44]. The resultant thin oxide film, with enhanced surface area and thickness, exhibited a higher photocurrent density. What is more, the annealing temperature and crystallite of the as-anodized WO_3 nanostructures was found as a critical factor e. g. in water splitting reaction[44]. Despite many reports describing synthesis approach of WO_3 nanostructures with electrochemical method, there is still lack of knowledge about the effect of synthesis parameters (such as electrolyte composition, applied potential and time period duration) on the geometrical parameters, optical and photocatalytic properties with photoactivity of the WO_3 nanoflowers.

Motivated by this, we propose, for the first time, a novel synthesis method of the self-assembly three-dimensional tungsten oxide nanoflowers (3D WO_3 NFs) thin film with improved optical and photoelectrochemical properties and exhibited enhanced photocatalytic activity in the reaction of toluene degradation under visible irradiation. The objectives of the present study are, therefore: *(i)* to optimize synthesis conditions of the WO_3 NFs, *(ii)* to correlate morphological dimensions and photoactivity and *(iii)* to find optimal synthesis conditions to assure that the nanostructures do not decompose under illumination and its remains stable in time.

2. Materials and Methods

2.1 Materials

Isopropanol (p.a., POCh. S.A., Gliwice, Poland), acetone, methanol (p.a., P.P.H. STANLAB, Lublin, Poland) and deionized water (DI, with conductivity of 0.05 μS) were used during sonication process. WO_3 NFs were synthesis with using anodic oxidation of tungsten foil (0.127 mm, 99.9% purity, Sigma Aldrich, Sigma Aldrich) in the aqueous electrolyte composed of sulphuric acid solution (96%, p. a., P.P.H. STANLAB, Lublin, Poland) and sodium fluoride (p. a., P.P.H. STANLAB, Lublin, Poland).

2.2 Synthesis of WO_3 nanoflowers

W foils were cut into 2 x 2 cm samples and ultrasonically cleaned in acetone, isopropanol, methanol and deionised water for 10 minutes in each solvent and then dried in an air stream[45,46]. The as-cleaned samples were contacted with a Cu spring and pressed against an O-ring in an anodization cell, which consists of a two-electrode configuration with W foil as the working electrode (anode) and the platinum foil as the counter electrode (cathode). All the experiments were performed at room temperature. The electrolytes containing various concentration of sodium fluoride (0.1, 0.2, 0.5, 0.7 and 1.0 wt.%) and sulphuric acid (0.5, 1 and 1.5 M) were used. A sets of analysis were conducted for 15, 30, 45, 60, 90 and 120 minutes during anodization at the voltage range of 10 – 50 V using programmable power supply (MCP M10-QS1005). The as-anodized samples were raised with deionized water, dried overnight at 60℃ and then annealed at 400℃ for 4 h with a ramping rate of 4℃/min in the air environment.

2.3 Material characterization

A high resolution scanning electron microscopy (HRSEM, JEOL, JSM – 7610F) was used to analysed the morphology parameters of WO_3 NFs. Cross-sectional images were obtained in which the samples were scrunched and measured at the angle of 30° tilted view to determine the thickness of the films. The crystal structure of the samples was determined from X-Ray diffraction patterns recorded in the range of $2\theta = 20 – 80°$, using an X-Ray diffractometer (XRD, Rigaku MiniFlex 600) with Cu Kα radiation. UV-Visible absorption spectra of the samples in the wavelength of 200 - 800 nm were collected by using diffuse reflectance UV−Vis spectroscopy (Thermo Scientific) equipped with an integrating sphere with baseline determined with barium sulphate as reference. The photoluminescence (PL) measurements were carried out at room temperature using a photoluminescence spectrometer LS-50B (PerkinElmer) equipped with Xenon discharge lamp as an

excitation source and a R928 photomultiplier as detector. The excitation radiation (300 nm) was directed on the surface of the samples at an angle of 90°. The Raman spectra were collected with a Thermo Scientific DXR Smart Raman spectrometer with a 532 nm laser as the excitation source under ambient conditions.

2.4 Photocatalytic performance

The photocatalytic activity of the as-prepared WO_3 thin films was tested by the visible-light-driven degradation of toluene (200 ppm) from an air mixture, used as a model contaminant. The measurements were carried out in a flat stainless steel reactor of a volume of ca. 35 cm^3 equipped with a quartz window, two valves and a septum. The irradiation source consisted of a LED array with λ_{max} = 415 nm was located above the sample. The as-anodized foil was placed at the bottom side and the reactor was closed with a quartz window. Subsequently, the gaseous mixture was passed through the reactor for 1 min. Then, the valves were closed and the reactor was kept in dark for 30 min in order to achieve equilibrium. Before starting the irradiation, a reference toluene sample was taken. The concentration was determined by using a gas chromatograph (TRACE 1300, Thermo Scientific), equipped with an ionization flame detector (FID) and a Phenomenex capillary column (30 mm x 25 mm, 0.5 μm). The samples (200 μL) were dosed with a gastight syringe each 10 min. Intensity of irradiation was measured by an optical power meter and reached 15 mW/cm^2.

2.5 Photoelectrochemical activity

Photocurrent measurements were performed using an AutoLab PGSTAT 204 potentionstat-galvanostat (Methrom) with the three-electrode system. Prepared samples were used as working electrodes with Ag/AgCl/0.1 M KCl and Pt mesh as the reference and counter electrodes, respectively. The active surface area of the electrode was 0.25 cm^2. Prior to the measurement, the electrolyte 0.1 M Na_2SO_4 water solution, was purged with argon for 1 h. Similarity, the space above the electrolyte during the measurements was purged with argon. Photocurrent measurements under UV-Vis and visible irradiation were analyzed using a 250 W Xe light source with a 420 nm cut-off filter (for visible light irradiation).

3. Results

To investigate the effect of the synthesis conditions and electrolyte composition, (anodization potential, reaction time, concentration of H_2SO_4 and NaF) on the morphological, photoactivity and photoelectrochemical properties of the anodic oxide WO_3, a series of the samples were prepared. The labels of the as-prepared samples together with the synthesis conditions, morphological parameters, optical band gap and efficiency of toluene degradation are presented in Table 1.

179

Table 1. Sample label, morphology parameters, optical band gap and efficiency of toluene degradation of the obtained samples.

Sample label	Preparation conditions (electrolyte composition and anodization parameters)		Flower diameter (nm)	Oxide layer thickness (μm)	Platelets thickness (nm)	Optical band gap (eV)	Efficiency of toluene degradation after 60 minutes of irradiation (%)
	Constant parameters	Variable parameters					
WO_10 V	1.0 M H_2SO_4, 0.5 wt.% NaF, 90 min	10V	-**	0.1±0.1	11.8±0.1	2.75	36
WO_20 V	1.0 M H_2SO_4, 0.5 wt.% NaF, 90 min	20V	-**	0.3±0.1	12.8±0.2	2.61	67
WO_30 V	1.0 M H_2SO_4, 0.5 wt.% NaF, 90 min	30V	0.72±0.1	0.8±0.1	13.6±0.2	2.65	90
WO_40 V*	1.0 M H_2SO_4, 0.5 wt.% NaF, 90 min	40V	1.21±0.1	1.05±0.1	14.9±0.3	2.52	100
WO_50 V	1.0 M H_2SO_4, 0.5 wt.% NaF, 90 min	50V	0.81±0.2	1.2±0.1	16.9±0.3	2.65	73
WO_15 min	1.0 M H_2SO_4, 0.5 wt.% NaF, 40V	15 min	-**	0.1±0.02	11.2±0.1	2.66	15
WO_30 min	1.0 M H_2SO_4, 0.5 wt.% NaF, 40V	30 min	0.91±0.1	0.3±0.05	12.3±0.1	2.64	25
WO_45 min	1.0 M H_2SO_4, 0.5 wt.% NaF, 40V	45 min	1.04±0.2	0.5±0.1	13.1±0.2	2.56	55
WO_40 V*	1.0 M H_2SO_4, 0.5 wt.% NaF, 40V,	90 min	1.21±0.1	1.05±0.2	14.9±0.2	2.52	100
WO_120 min	1.0 M H_2SO_4, 0.5 wt.% NaF, 40V	120 min	1.52±0.2	1.35±0.1	15.6±0.2	2.40	78
WO_0.5 M H_2SO_4	0.5 wt.% NaF, 40V, 90 mi	0.5 M H_2SO_4	1.15±0.1	1.17±0.1	13.4±0.2	2.63	86
WO_40 V*	0.5 wt.% NaF, 40V, 90 min	1.0 M H_2SO_4	1.21±0.1	1.05±0.1	14.9±0.2	2.52	100
WO_1.5 M H_2SO_4	0.5 wt.% NaF, 40V, 90 min	1.5 M H_2SO_4	1.10±0.1	1.0±0.1	15.3±0.3	2.55	90
WO_0.1 wt.% NaF	1.0 M H_2SO_4, 40V, 90 min	0.1 wt.% NaF	-**	1.0±0.01	11.3±0.1	2.79	26
WO_0.2 wt.% NaF	1.0 M H_2SO_4, 40V, 90 min	0.2 wt.% NaF	-**	1.02±0.1	12.1±0.2	2.62	61
WO_40 V*	1.0 M H_2SO_4, 40V, 90 min	0.5 wt.% NaF	1.21±0.1	1.05±0.01	14.9±0.3	2.52	100
WO_0.7 wt.% NaF	1.0 M H_2SO_4, 40V, 90 min	0.7 wt.% NaF	-**	1.1±0.01	15.9±0.3	2.55	86
WO_1.0 wt.% NaF	1.0 M H_2SO_4, 40V, 90 min	1.0 wt.% NaF	-**	1.15±0.01	17.8±0.3	2.66	74

*The WO_40 V sample was synthesised in the following conditions: 90 min, 40 V, 0.5 wt.% NaF and 1.0 M H_2SO_4 in each series to compare the influence of preparation conditions.

**The formation of the flower buds was not observed.

3.1. Morphology

3.1.1 Effect of the anodization potential

Series of samples in the range of 10 to 50 V were synthesized to determine the effect of the anodization potential on the growth of the WO_3 nanostructure. The results are displayed in Figure 1. Too low anodization potential (below 20 V) resulted in the formation of the anodic oxide layer possessing platelets nanostructure. Its irregular shape has been gradually transformed into flower-like structure when the anodization potential increased to 30 V and revealed growth of the irregular, sparsely spread flower buds with the diameter of 0.72 ± 0.1 nm. Regular shape and repeatable distribution were observed for the sample anodized at 40 V with the diameter of the flowers buds equaled 1.21 ± 0.1 μm. However, further increase to 50 V caused decrease of the flowers buds abundance (see Figure 1). Decrease in the diameter of WO_50 V to 0.81 ± 0.2 nm was also observed. Moreover, it was found that the nanoplatelets started to deform – were rounded and looked like developed buds. On the other hand, increasing the anodization potential resulted in an increase in the oxide layer thickness and platelets thickness from 0.1 ± 0.1 μm and 11.8 ± 0.1 nm for the WO_10 V sample to 1.2 ± 0.1 nm and 16.9 ± 0.3 nm for WO_50 V, respectively. Additionally, higher applied voltage resulted in sharpening the edges of the nanoplatelets.

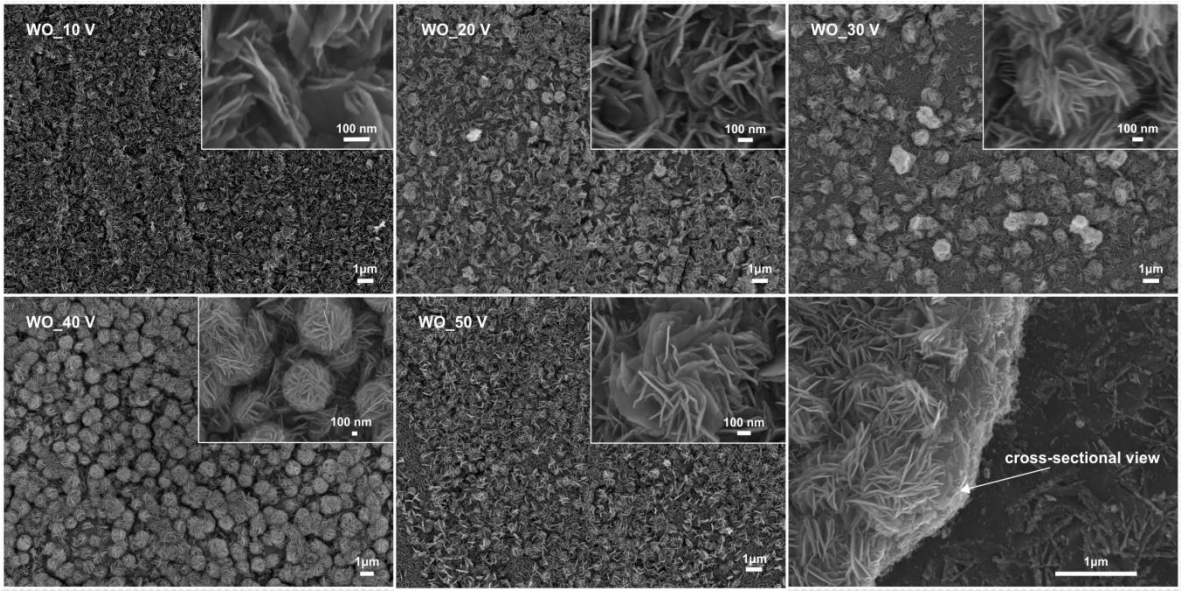

Figure 1. Effect of the anodization potential on the morphology of WO_3 NFs. Fluoride content 0.5 wt.%, H_2SO_4 concentration 1.0 M, anodization time 90 min.

3.1.2 Effect of the anodization time

To investigate the effect of the anodization time on the growth of the nanoflowers, a series of experiments were conducted for different durations and the results are presented in Figure 2. The sample anodized at 40 V has been chosen to explore further its anodization time because it exhibited the most ordered, regular shape of flower-like structure. It established that the obtained layers consisted of irregular buds when the anodization time decreased below 90 minutes. Moreover, in shorter time fewer pores were formed and an increase in heterogeneity of the layers was observed. It could be assume that the growth of well-ordered flowers buds require soluble species which are formed by the initial anodic growth of the oxide layer, which will be further discussed in this paper. We suggest that the continuously increase in the anodization time allows to achieve steady state while the diameter of the flower buds, the thickness of the oxide layer and the platelets thickness were still improved. Diameter increased to 1150 nm, oxide layer thickness from 0.1 ± 0.02 to 1.35 ± 0.1 μm, and

platelets thickness from 11.2 ± 0.1 to 15.6 ± 0.2 nm, respectively for WO_15 min and WO_120 min (see Table 1). It was found the flowers buds were evenly distributed on the layer for the anodizing time of 90 min (Figure 2). However, further extension of the anodization time had an negative effect on the WO_3 nanostructures, whereby the regular flower-like nanostructure of WO_3 was destroyed and the anodic oxide was composed of irregular, poorly distributed flower buds. Moreover, slow transformation of the flower buds again into nanoplatelets was observed. The reason might be attributed to the higher etching rate on the WO_3 surface layer with extension of the anodization time up to 120 minutes (see Fig. 2). Similar observation of the flower-like structure growth with an extension of the anodization time was also studied and published by Amal group[29].

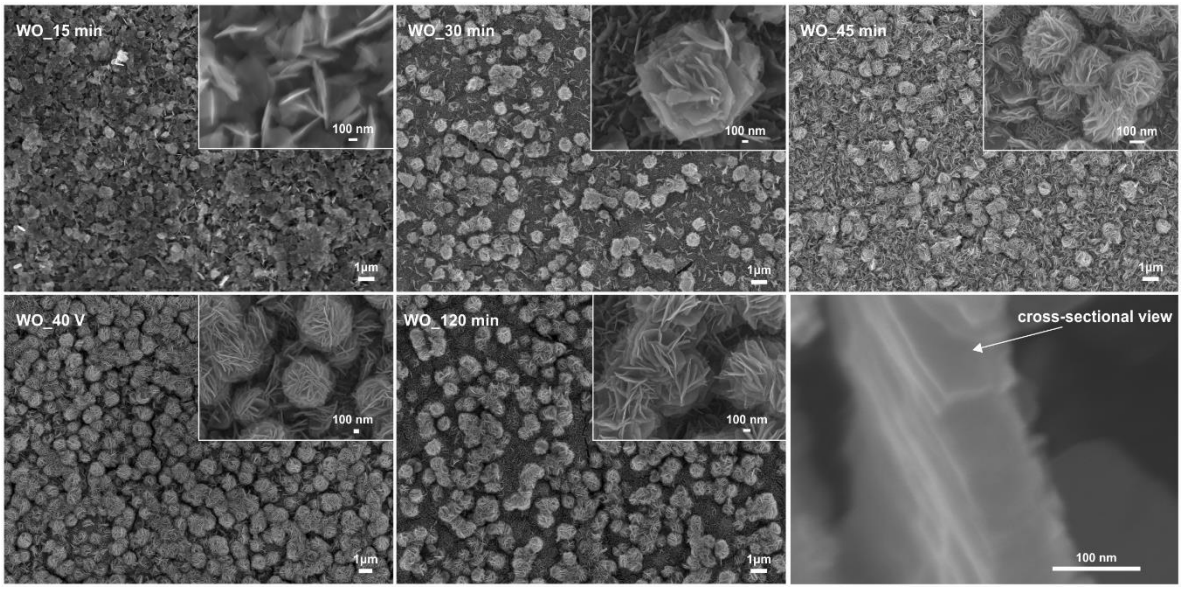

Figure 2. Effect of the anodization time on the morphology of the WO_3 NFs. Fluoride content 0.5 wt.%, H_2SO_4 concentration 1.0 M, anodization potential 40 V.

3.1.3 Effect of the sulphuric acid concentration

A significant impact of the sulphuric acid concentration on the homogeneity of the samples was noticed. Too low (0.5 M) or too high (1.5 M) concentration caused disorganization of the nanoplatelets forming the oxide layer. Moreover, for the both mentioned concentrations, the layers consisted of evenly distributed nanoplatelets with poorly formed irregular buds. According to the literature, for the initial oxidation step occurs, the W foil needs to be in contact with the oxidizing acid which initially oxidize into WO_2^{2+} and results in the formation of the continues oxide film[29,43]. However, we assume that loo low acid concentration resulted too slow nucleation rate (WO_0.5 M H_2SO_4). Furthermore, it was found that the increase in the acidity of the environment resulted in etching of the ions WO_2^{2+} ions as it was confirmed from the Pourbaix diagram [47] and thus less distributed flower-buds were observed (see Figure 3). El-Basiouney *et al.* also concluded that the dissolution of WO_3 oxide layer in acidic medium takes place, which is consistent with the below proposed mechanism. The optimal concentration for forming regular flower buds was 1.0 M reaching the highest diameter of 1.21 ± 0.1 nm. The increase of the acid concentration had a slight influence on the oxide layer and platelets thickness, the changes from 1.17 ± 0.1 to 1.0 ± 0.1 μm and from 13.4 ± 0.2 to 15.3 ± 0.3 nm, respectively for WO_0.5 M H_2SO_4 and WO_1.5 M H_2SO_4, were observed.

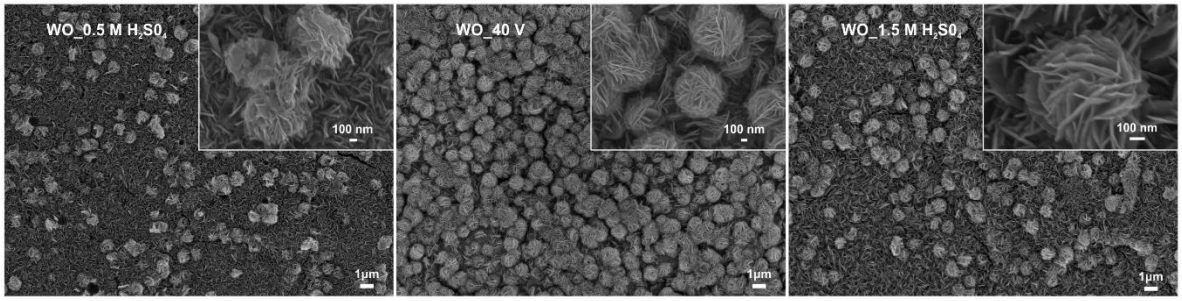

Figure 3. Effect of the sulphuric acid concentration on the morphology of WO_3 NFs. Fluoride content 0.5 wt.%, anodization potential 40 V, anodization time 90 min.

3.1.4 Effect of the sodium fluoride concentration

The effect of fluoride content concentration was investigated by the anodization of the samples at 40 V for 90 minutes in the electrolyte containing 0.5 M H_2SO_4 in the range of 0.1 to 1.0 wt.% NaF. The small content of F^- ions resulted in a growth of the layers consisted of the regular nanoplatelets (0.1 wt.%). The self-assembly flower buds have already occurred at 0.2 wt.% NaF content. Regularly formed buds were found for the WO_0.5 wt.% NaF sample with the diameter equalled 1.21 ± 0.1 nm. Further increased of the NaF concentration led to deformations of the flowers buds morphology to single, packed nanoplatelets. Moreover, the results revealed that with the increasing amount of NaF concentration, increase of sharpened edges of the nanoplatelets was observed. The oxide layer and platelets thickness increased slightly from 1.0 ± 0.01 to 1.15 ± 0.01 μm and from 11.3 ± 0.1 to 17.8 ± 0.3 nm, respectively for WO_0.1 wt.% NaF and WO_1.0 wt.% NaF, implying that the NaF concentration was mainly responsible for the flower buds formation.

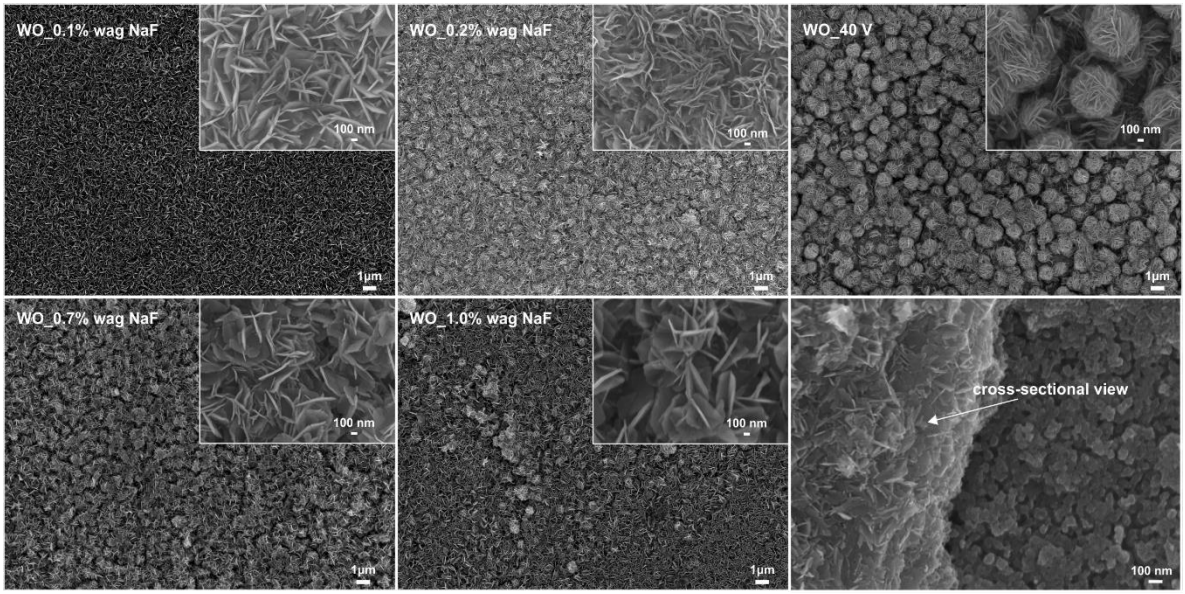

Figure 4. Effect of the sodium fluoride concentration on the morphology of theWO_3 NFs. H_2SO_4 concentration 1.0 M, anodization potential 40 V, anodization time 90 min.

Similarly to the formation of the anodized titanium dioxide nanotubes films (TiO_2 NTs) in the electrolyte containing fluorine ions[48,49], the WO_3 NFs films were formed as a result of field-assisted oxide growth and localized chemical dissolution. Based on the above results and literature reports[28,29,50], we propose the following mechanism of the WO_3 NFs thin film growth process: *(i)* formation of a dense oxide layer on W foil, *(ii)* activation of the barrier oxide layer by fluoride ions resulting in chemical dissolution of the oxide layer and *(iii)* deepening of the oxide pits that in time branch out formation flower shaped nanostructures (Scheme 1). The proposed schematic illustration of the anodic growth of oxide layer is presented on Scheme 1 according to the following equations:

$$W + H_2O \rightarrow WO_2^{2+} + 4H^+ + 6e^-, \quad (1)$$

$$2WO_2^{2+} + H_2O \rightarrow W_2O_5 + 2H^+ + 2e^-, \quad (2)$$

$$W_2O_5 + H_2O \rightarrow 2WO_3 + 2H^+ + 2e^-, \quad (3)$$

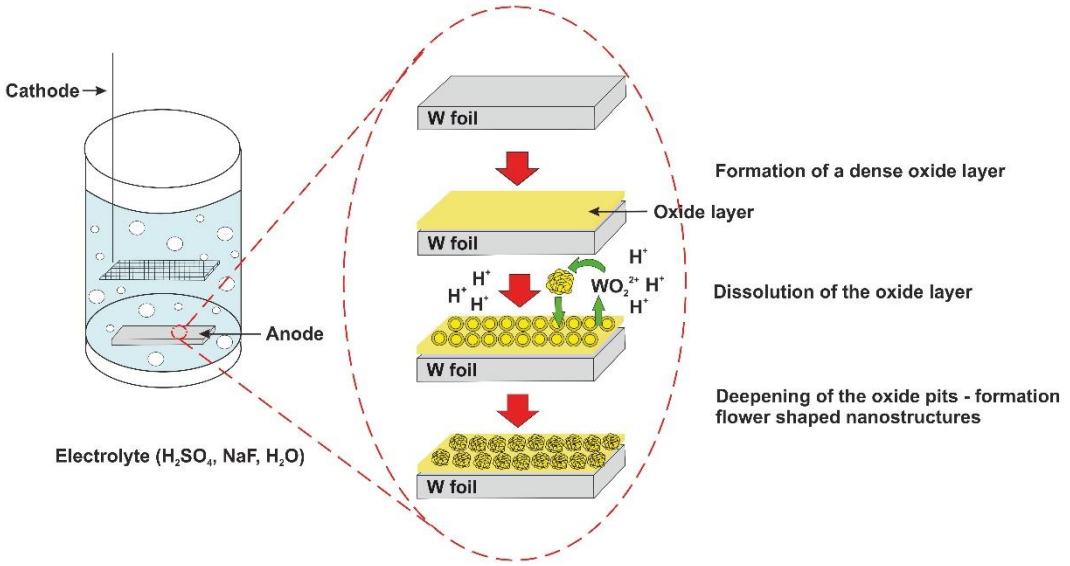

Scheme 1 Schematic illustration of the WO_3 NFs thin film growth process.

Reaction 1 describes the electrochemical dissolution of tungsten foil and formation of an oxide layer of WO_2^{2+} on the surface. Subsequently, the WO_2^{2+} ions are attracted by water molecules and form an intermediate W_2O_5 oxide. Since the WO_2^{2+} and intermediate W_2O_5 are decomposed in an aqueous environment, the oxide layer growth. Further oxide growth is controlled by the field enhanced ion transport through the growing oxide. This process is self-limiting under a constant applied voltage, as the field within the oxide layer is progressively reduced by the increasing oxide thickness, thus resulting in the growth of a compact WO_3 film with finite thickness. During the initial step, disordered pits are formed and a nanoporous structure is subsequently developed by the chemical dissolution of the oxide layer or the direct complexation of WO_2^{2+} at the oxide electrolyte interface and form soluble fluoride complexes[49]. The anodic growth of the WO_3 oxide layer became a competition between its and the chemical dissolution of the tungsten oxide layer in a fluoride containing electrolyte solution[51,52]. During the anodization process, the constant growth and chemical dissolution of the tungsten oxide layer occurs simultaneously and a steady state is established when the growth rate at the metal oxide interface occurs at the same as the dissolution rate of oxide film at the outer interface[13,28].

As mentioned above, the anodic growth of the compact oxide on the metal surface and the formation of pores is governed by chemical dissolution of the formed oxide layers induced by fluoride ions from the electrolyte solution and formation of a soluble fluoride complex. The key point is to find an optimize amount of the fluoride content, needed to form a porous structure, allows for the successful formation of the flower-like structure. Too low or too high concentration revealed presence of the nanoplatelets instead of nanoflowers (see Figure 4) indicating that the presence of fluoride ions is essential to generate soluble ions (WO_2^{2+}) and form the flower-like structure. Moreover, an increase in the NaF concentration (to 1.0 wt.%) resulted in slowly etching of the oxide

layer and exhibited poorly organized flowers buds co-existence together with nanoplatelets (see Figure 2). Lai [53] also investigated the influence of the fluoride content on the growth of anodic WO_3 nanotubular structure and realised that optimization of fluoride ions played crucial role in controlling formation the chemical dissolution reaction on the interface of W/WO_3 and thus growth of the nanotubes. It should be remarked that dissolution of WO_3 occurs over the entire W foil, thus with extending oxidation time we observed gradual transformation of the nanoplatelets info flower-like structure after 90 minutes of the anodization process. Further time extension resulted in an opposite effects (Figure 2). Moreover, literature survey reports that the dissolution of WO_3 in acid medium takes places *via* the formation of WO_2^{2+} species[54]. Therefore, it might lead to the precipitation of primary formed WO_2^{2+} and allows for thickening of the WO_3 nanostructured film. However, we observed that the increase of the acid concentration resulted in the formation of slightly thinner oxide layer (see Table 1). Therefore, we assume that the dissolution of the oxide layer could be driven by the instability of WO_2^{2+} in the presence of aqueous electrolyte solution at room temperature and presence of high anodization potential.

3.2 Crystallographic structure

Figure 5 displays the X-ray patterns of the self-assembled WO_3 NFs film. The reflection patterns of the WO_3 could be indexed to a triclinic phase. The WO_3 phase was represented by the peaks (001), (020), (200), (101), (111), (021), (221) and (400) crystal planes at 2θ located around 23.3°, 23.8°, 24.4°, 26.8°, 28.9°, 33.8°, 41.4° and 50.5°. The peaks indexed to W foils were found at 2θ of approximately 52.5 (denoted in Figure 5 "*"), 58.5 and 73.4 . The XRD patterns of the samples anodized for 90 minutes in the potential range of 10 – 50 V are given in Figure 5a. As noted, the potential of 10 V was too low for successful formation of the oxide layers thus it was hard to establish any of the peaks in range of 23 -25°. It was found that with increasing anodization potential the intensity of the peak (200), characteristic for triclinic phase of WO_3, increased. However, further rise to 50 V resulted in the intensity decrease. As the anodization time increased we observed that the intensity of the (001) peak decrease whereas the (200) one stared to intensively arise and reached its highest intensity with an oxidation time of 120 minutes (see Figure 5b). As the sulphuric acid concentration increased, the intensity of the (200) peak started to decrease whereas the intensity of peaks indexed to (001) and (020) became higher (Figure 5c). An optimum concentration which allowed for the growth of the oxide layer was 1.0 M. Interestingly, concentration of fluoride content strongly affected on the peaks height indexed to WO_3 (Figure 5d). Only the WO_0.5 wt.% NaF sample revealed the presence of the peaks (001), (020), (200), (101) and (111), whereas the rest of the samples in this series possessed the intensive peak indexed to (200). Reduction of the (001) peak and thus enhancement of the (200) peak intensity in all the samples could be ascribed to the improvement of the nanostructured layer and compact oxide layers obtained at different conditions. The WO_3 NFs samples possessed analogous crystallinity, while different synthesis conditions resulted in changes of the refined lattice parameters a, b, and c as well as unit cell volume, which are gathered in Table S1.

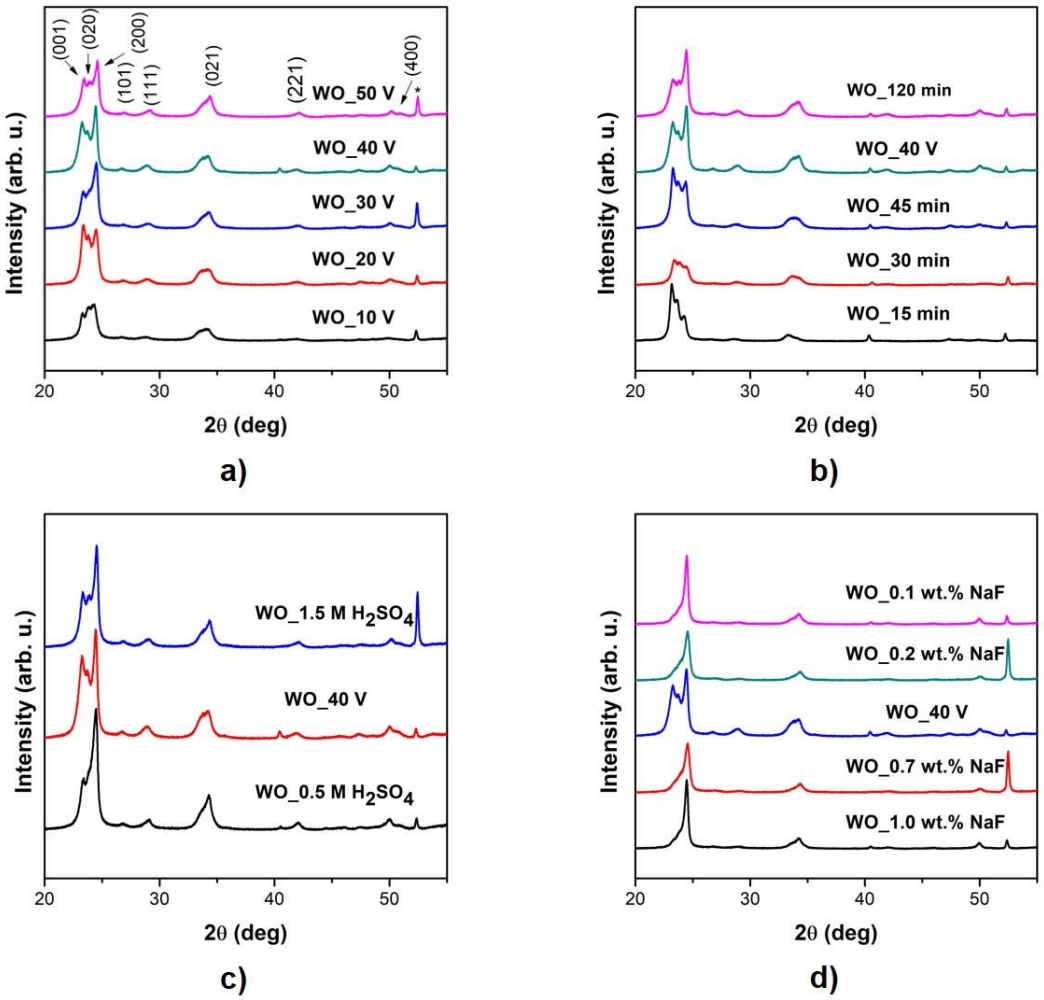

Figure 5. XRD patterns of the WO_3 NFs samples differing in (a) applied potential, (b) anodization time, (c) H_2SO_4 and (d) NaF concentration.

The Raman spectra of the samples are displayed in Figure 6. As it can be seen, we can determine three frequency regions. The first one appeared at lower frequencies (below 200 cm^{-1}) in regards to the relative translational or rotational motions of the WO_6 octahedral. The second region occurs between wave numbers of 200 – 400 cm^{-1} indicating the O-W-O bending mode. The last region with peaks located at around 600 – 900 cm^{-1} is indexed to the O-W-O stretching modes[55]. The Raman spectra confirmed the WO_3 triclinic phase due to the presence of the characteristic peaks at around 144, 194, 269, 324 713 and 807 cm^{-1}. No Raman signal corresponding to the tungsten was observed. The bands of 269 and 324 cm^{-1} can be attributed to the δ bending (O-W-O) and ν (W–O–W) vibrations modes of the bridging oxygen[56]. The strongest peaks observed at 713 and 807 cm^{-1} can be assigned to the stretching modes arising from O-W-O[23,56]. All the samples exhibited the same features but as the preparation conditions changed, an intensity of the peaks starts to arising (especially at around 269 and 807 cm^{-1}) indicated the formation of the oxide layer (see Figure 6 a-d).

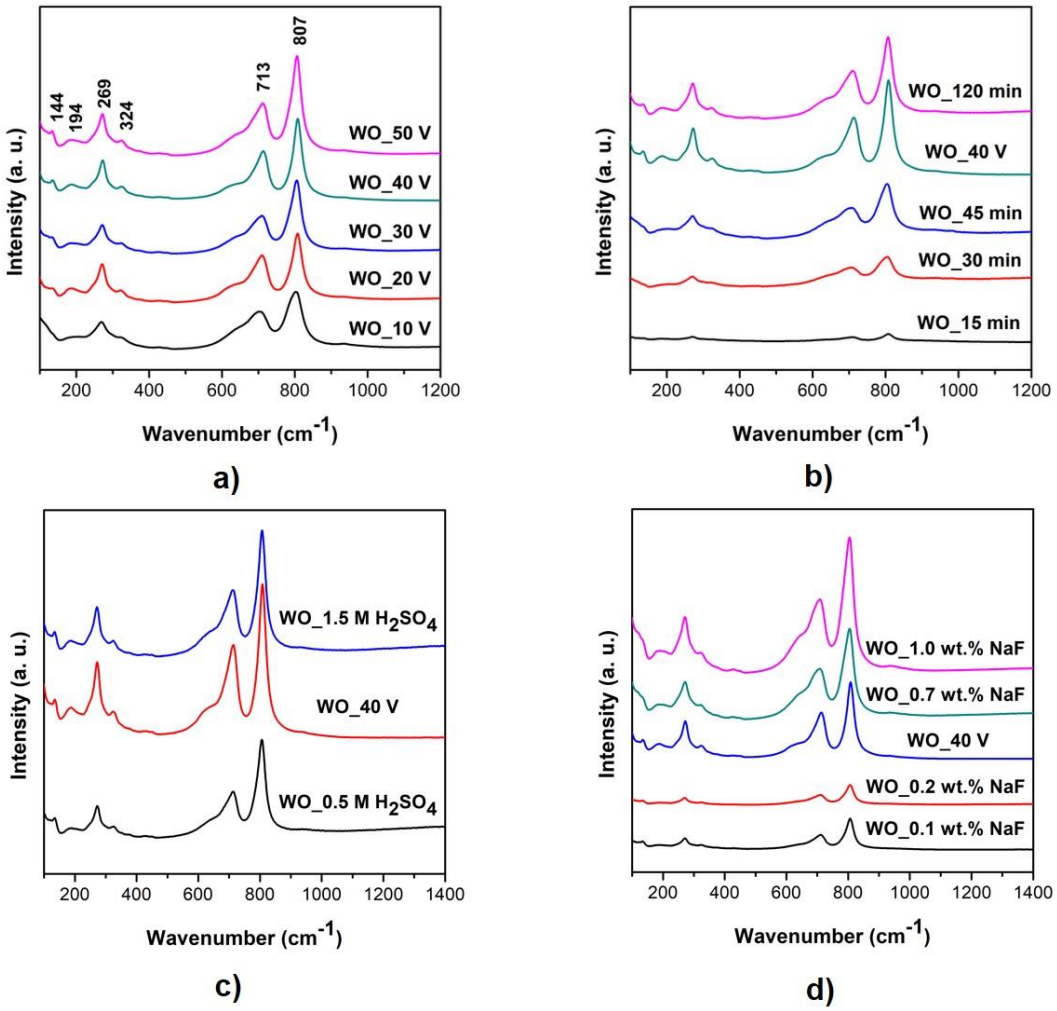

Figure 6. Raman spectra of the WO_3 NFs samples differing in (a) anodization potential, (b) anodization time (c) H_2SO_4 and (d) NaF concentration.

3.3. Optical and photoluminescence properties

The change in the optical properties of the as-prepared WO_3 films by the photoabsorption studies (Figure S1) and corresponding optical bang gap energy as presented in Figure 7 were investigated. The absorption edge of the series differ in the applied potential was located approximately of 470 nm for all samples (Figure S1a). As the anodization time increase from 15 to 120 minutes the absorption edge shifted from 460 to 540 nm (see Figure S1b), respectively. Higher acid concentration practically did not influence on the absorption edge which was around 475 nm (Figure S1c). For the series differing in fluoride ions concentration, the absorption edge was around 450 nm for all sample except the one obtained with the lowest amount of NaF (0.1 wt.%) – approximately 430 nm (Figure S1d). An absorption shift in the 450 – 800 nm range was observed for all samples, confirming changes in the structure of the obtaining samples. Raised absorbance values at higher wavelengths could be attributed to the presence of oxygen vacancies on the surface film. Furthermore, it was found that as the anodization time increased the photoabsorbance values decreased due to decrease in amount of suboxides and oxygen vacancies. A similar observation was described by Amal et al. who analysed the influence of duration time period on the flower-shaped WO_3 growth[29].

The band gap of WO_3 NFs films can be determined by considering the indirect transition between 2p electrons from the valence band (VB) of oxygen and the 5d the conduction band (CB) of tungsten based on the Tauc's plot according to the following equation[57,58]:

$$\alpha h\nu = A(h\nu - E_g)^n, \quad (4)$$

where α, ν, A and E_g are absorption coefficient, light frequency, proportionality constant, and band gap, respectively. The band gap energies of the WO_3 NFs samples were calculated with equation 4 and the data were collected in Table 1 and displayed on Figure 7. The values were in accordance with the literature, where the band gap values for the flower-shaped WO_3 film was around 2.5 - 2.75 eV[37,40].

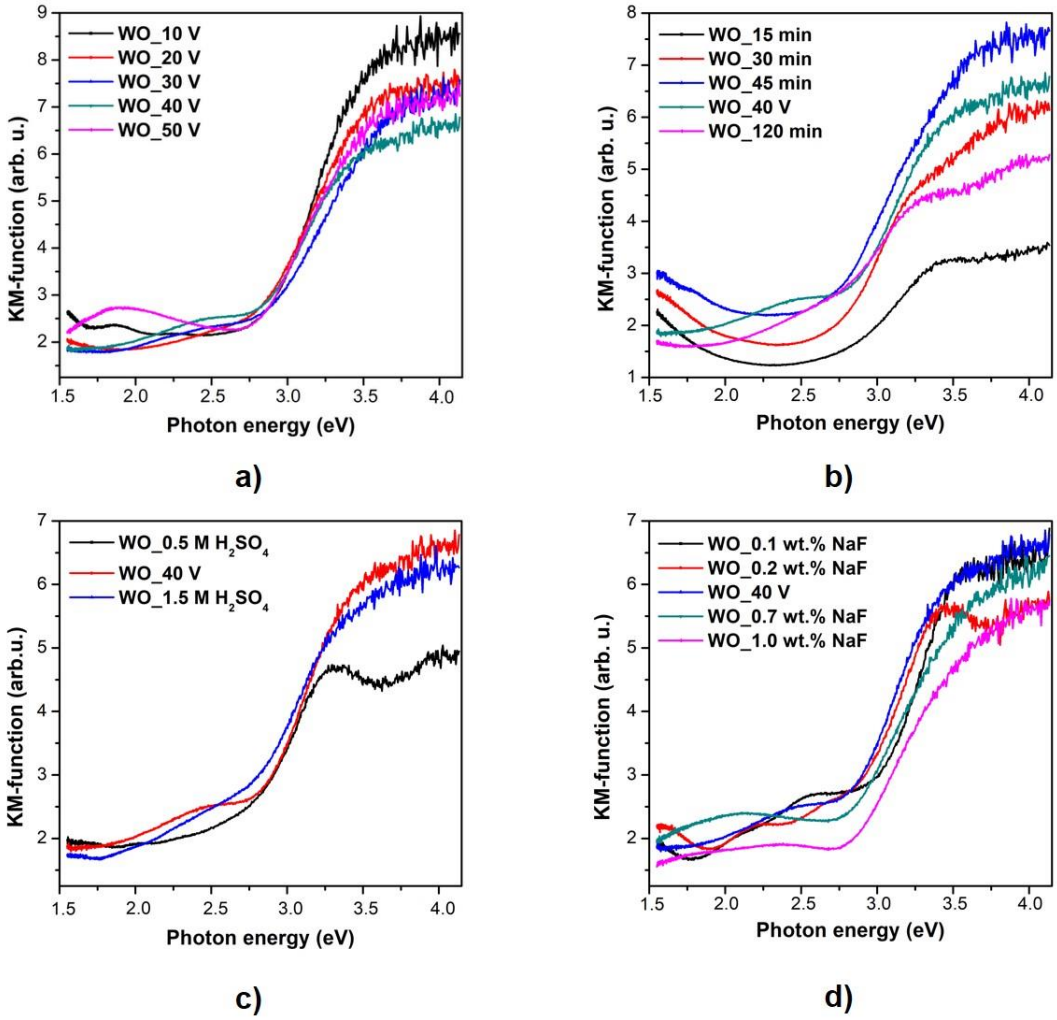

Figure 7. Optical band gap spectra of the WO_3 NFs samples differing in (a) anodization potential, (b) anodization time (c) H_2SO_4 and (d) NaF concentration.

Photoluminescence spectra for the as-obtained WO_3 NFs samples in four different series are shown in Figure 8 a-d. Typically for the oxygen metal based semiconductors, the PL spectra are composed of UV emission and a visible emission band attributed to the surface defects. All the samples exhibited the same PL features with different intensity depending on the preparation conditions. The emission was positioned at around 420, 438, 481 and 527 nm. The values at around 420, 438 and 481 nm might be attributed to the presence of intrinsic defects such as oxygen vacancies giving rise to donor states located below the CB. The emission located at wavelength of 527 nm

indicated the possibility of band recombination (intrinsic states rather than surface states). The values are consistent with those reported for the others semiconductors, such as TiO_2 and ZnO[59,60].

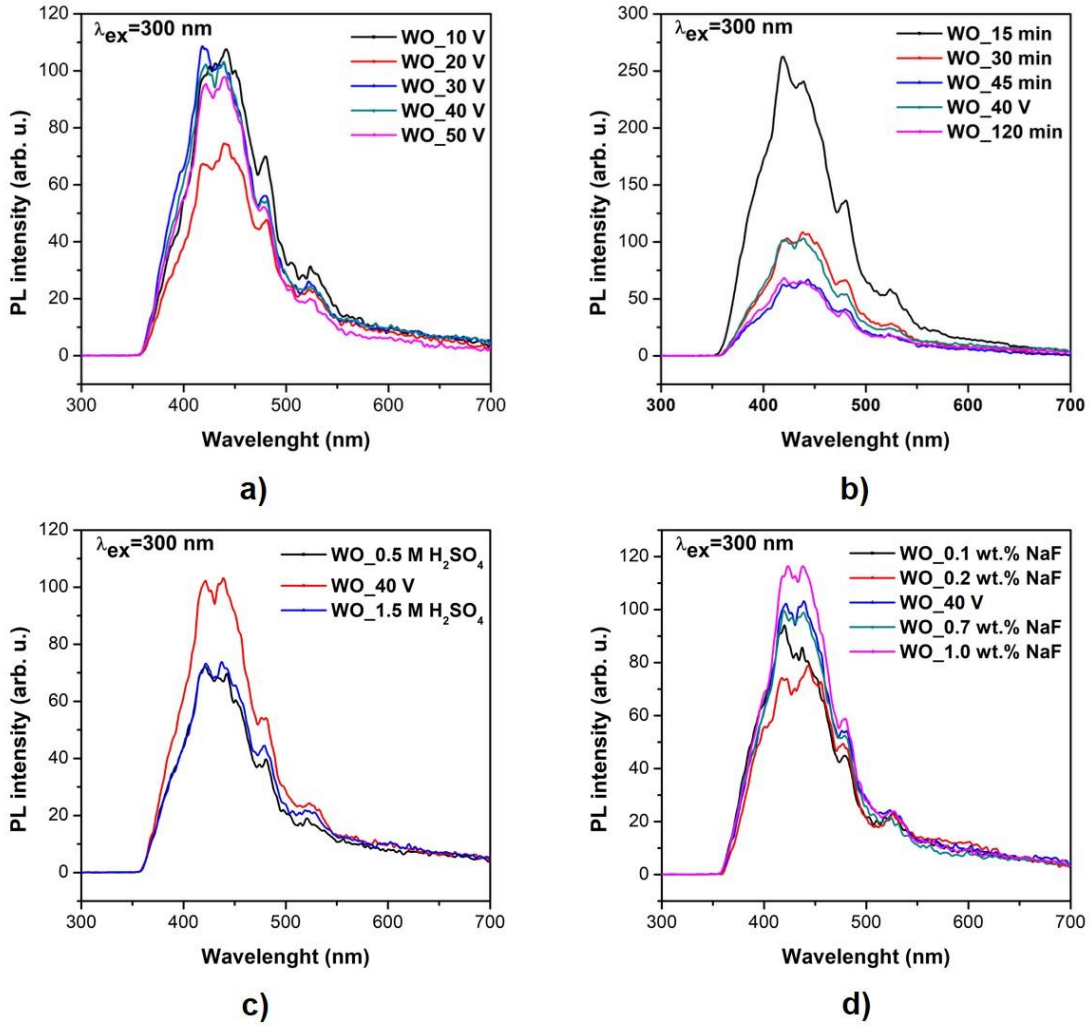

Figure 8 Photoluminescence spectra of the WO_3 NFs samples differing in (a) anodization potential, (b) anodization time (c) H_2SO_4 and (d) NaF concentration.

3.4 Photocatalytic activity

The potential environmental applications of the as-prepared WO_3 samples were investigated in a model reaction of toluene degradation from the air mixture to simple degradation products like CO_2 and H_2O. This approach was employed to analyse the effect of the preparation conditions, anodization potential and time, as well as electrolyte composition, concentration of sulphuric acid and sodium fluoride, on the WO_3 NFs photoactivity. The obtained results are displayed in Figure 9 and Table 1. It was found that samples preparation route by changing applied potential, anodization time and fluoride content significantly influenced the photocatalytic activity. In the case of different H_2SO_4 concentration, the samples WO_0.5 M H_2SO_4, WO_1.0 M H_2SO_4 and WO_1.5 M H_2SO_4 had comparable efficiency, 86%, 100% and 90%, respectively. As shown in Figure 9 a-d the highest photocatalytic activity, reaching 100% of toluene removal after 60 minutes of irradiation, achieved the sample prepared in the following conditions: anodization potential 40 V, anodization time 90 min, fluoride content 0.5 wt.% and H_2SO_4 concentration 0.5 M. Besides, further increase of the each parameter resulted in an opposite effect, decease of photoactivity was observed for WO_50 V, WO_120 min, WO_1.5 M H_2SO_4 and WO_0.1 wt.% NaF, 73%, 78%, 90% and 74%, respectively.

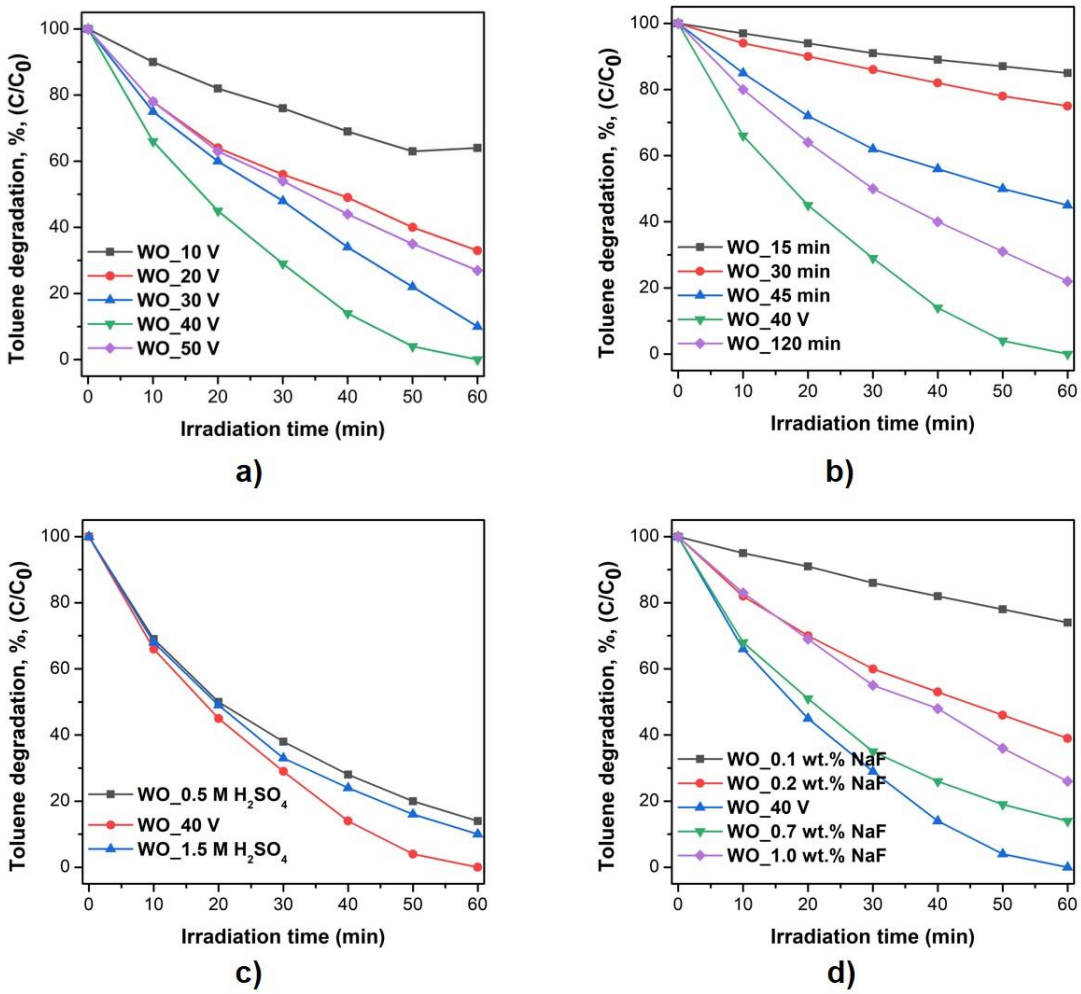

Figure 9 Photoactivity of the WO_3 NFs samples in gas phase degradation of toluene under Vis light irradiation (λ_{max} = 415 nm) differing in (a) anodization potential, (b) anodization time (c) H_2SO_4 and (d) NaF concentration.

In line with the other photocatalysts, the photoactivity of WO_3 depends on the lifetime of photogenerated charge carriers. Surface electron- hole recombination is extremely high with most of charge carriers recombining on the photocatalyst surface before the redox reactions and this recombination rate must be reduced in order to improve the photocatalytic activity. It seems that a simple toluene degradation route in presence of the WO_3 samples relies on the attack of the OH• radical to the methyl group of toluene. The key parameter that influence the improvement of the photocatalytic activity towards air pollutants degradation is morphology control. According to the literature, it was found that the flower-like three-dimensional (3D) structure photocatalysts possesses *(i)* larger surface area and *(ii)* plenty of mesopores with ordered open pore frameworks, into which photocatalyst may effectively harvest visible light due to multiple scattering[61,62]. Moreover, the large surface of flower-like structure could decrease the recombination efficiency of the photoexcited carries and favours their transfer to the surface to react with organic pollutants. When comparing the photoactivity of the as-prepared WO_3 samples with their morphological parameters, it was obvious that well-ordered, regular shape of nanoflowers array films were more efficient than the random occurred flowers buds or nanoplatelets (Table 1, Figure. 10). It could be ascribed to the more effective separation for the photogenerated electron-hole pairs and the larger surface area of the nanoflowers structure[63]. As apparent from the above discussed experimental data, the highest photocatalytic activity in the reaction of toluene decomposition (100%) after 60 min of LED irradiation (λ_{max} =

415 nm) was reached for the WO_40 V sample prepared in the following conditions: 40 V, 90 min, 1.0 M H_2SO_4 and 0.5 wt.% NaF. This sample also possessed the most uniform distribution and regular shape of the flowers buds with the diameter equalled to 1.21 ± 0.1 μm. We noticed that the efficiency of toluene degradation increased with increasing thickness of WO_3 array film, and then had a down trend (Fig. 10 a-d). The experimental results indicated that the 1.05 μm thick WO_3 film appeared with a maximum photodegradation efficiency of the toluene removal. Previous literature suggests that if the metal oxide thin film is thicker than the depth of light penetration, the bottom film absorbs only few incident photons and serves as an inter support and resulted in the decrease of the photocatalytic activity for a thick film[64].

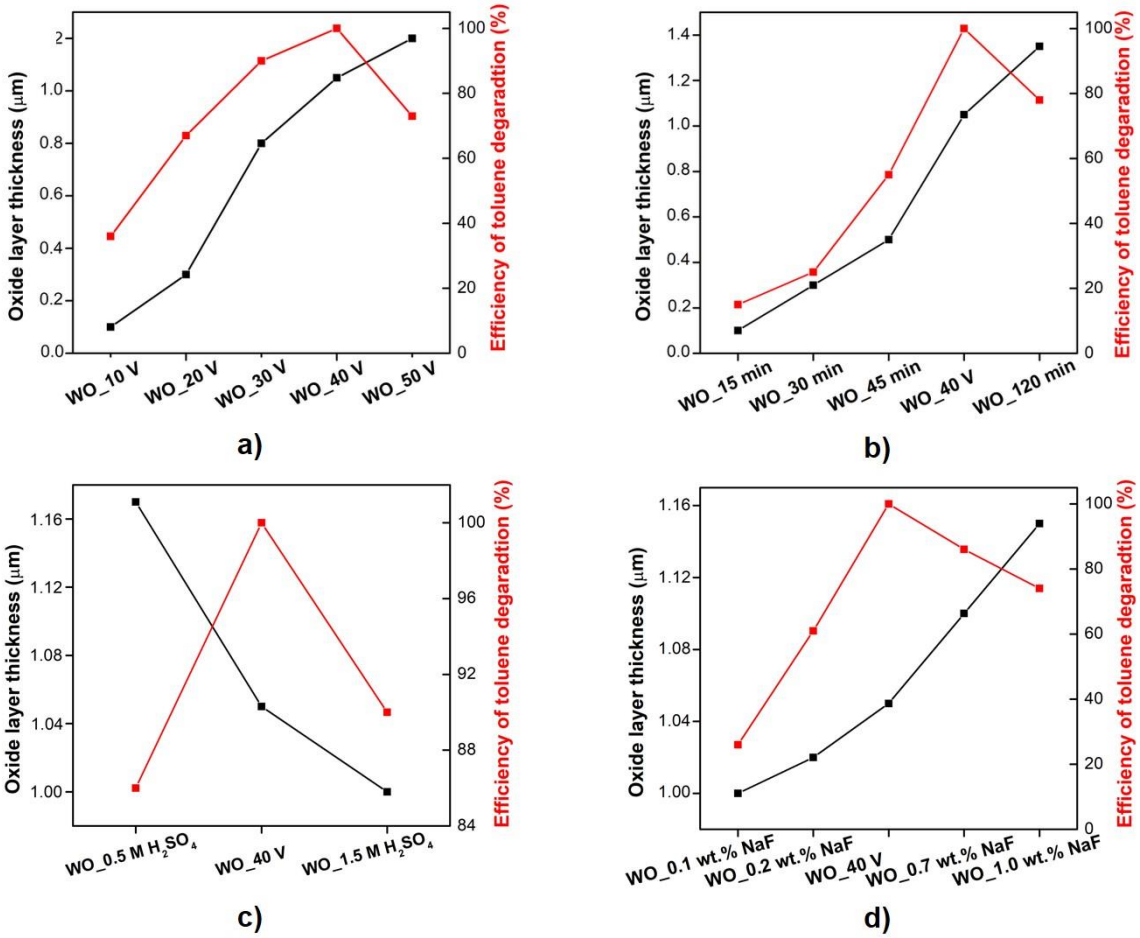

Figure 10. Influence of the oxide layer thickness on the efficiency of toluene degradation in the series differing in (a) applied potential, (b) anodization time, (c) H_2SO_4 and (d) NaF concentration.

3.5 Photoelectrochemical activity

Photoelectrochemical response of the samples prepared at different applied potential was evaluated as photocurrent measurements in light off/on cycles with 1.5 V applied voltage. Photocurrent was registered under both UV-Vis (Figure 11a) and Vis irradiation (Figure 11b). No significant decay of the photocurrent was observed during the photoelectrochemical measurements under both sources of irradiation indicating good stability of obtained photoelectrodes. The photocurrent under UV-Vis light was approximately 5 times higher in comparison with visible light irradiation. In addition, the same tendency in sample photoelectroactivity was observed for both types of light sources, namely as the anodizing voltage increased to 40 V, the measured photocurrent increased and then decreased (for a sample obtained at 50 V). This could be related to the high ordering of the platelet structure and the improvement of the nanostructured layer thickness with larger surface area which was achieving with increasing anodization voltage (up to 40 V). Prepared

448 samples, especially the most photoactive sample (WO_40 V), exhibited the large surface of flower-
449 like structure which increased the interface between oxide layer and electrolyte, facilitating incident
450 photons absorbance and the charge transfer for the separation of photoexcited hole – electrons pairs.

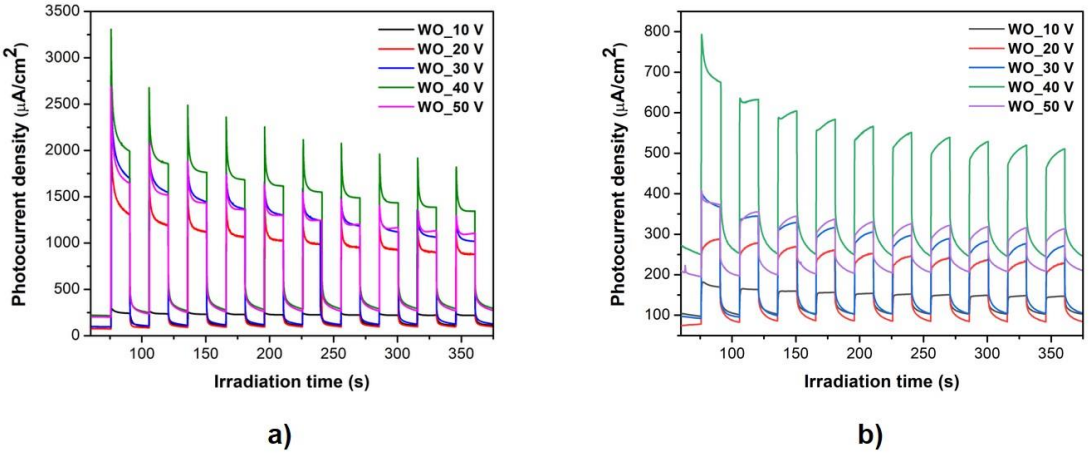

451

452 **Figure 11.** Photocurrent response of selected WO_3 samples under a) UV-Vis and (b) Vis irradiation
453 ($\lambda > 420$ nm) at 1.5 V in 0.1 M Na_2SO_4. The switch on/off period is 30 s.

454 **5. Conclusions**

455 In summary, we have described a simple and environmental friendly one-step anodization
456 synthesis method of the WO_3 NFs thin films in the aqueous solution containing fluoride ions. The
457 effect of synthesis conditions, applied potential and anodization time, as well as electrolyte
458 composition, concentration of H_2SO_4 and NaF contents, on the morphology, photocatalytic activity
459 and photoelectrochemistry properties of the WO_3 photocatalysts was presented. The results revealed
460 the growth of the nanoplatelets which were slowly transformed into the nanoflowers structure
461 depending on the synthesis parameters. The optimal conditions allowing the synthesis of the well-
462 organize, regular shaped flower buds with the diameter of 1.21 nm were: anodization potential of
463 40 V, anodization time 90 minutes, the electrolyte containing 1.0 M H_2SO_4 and 0.5 wt.% NaF. The
464 photocatalytic activity of the as-prepared WO_3 samples towards decomposition of air contaminants
465 was investigated in the model reaction of toluene degradation. Moreover, we found that the
466 morphology control was the key avenue to improve the photocatalytic activity. Hence, the samples
467 which consisted of the irregular shaped nanoplatelets exhibited lower photocatalytic activity than
468 those with the flower-like structure. The highest photoactivity in toluene degradation and in
469 photocurrent generation under UV-Vis and Vis irradiation achieved the sample with the most
470 ordered and regular flower buds, WO_40 V. Moreover, we noticed that the thickness of the oxide
471 layer was directly related with the photocatalytic efficiency. The thicker WO_3 layer was, the higher
472 decline in the photoactivity was observed because of difficulties of light penetration into deeper
473 layers. Although, the highest photoactivity exhibited the sample with thick of 1.05 μm (100%,
474 WO_40 V) and further increase of the oxide layer thickness resulted in an opposite effect. These
475 finding suggest that self-assembly, regular shape flower-like WO_3 thin film activated with low-
476 powered LEDs as an irradiation source (λ_{max} = 415 nm) could be a promising material for air
477 purification. The synthesis of visible light active and stable photocatalyst can boost the technology of
478 air purification since they exploit a renewable energy source and allow to avoid an extra operational
479 costs and other limitations associated with artificial illumination.

480 **Supplementary Materials:** Figure S1: Photoabsorption spectra of the WO_3 NFs samples from four series each
481 with a different (a) applied potential, (b) anodization time, (c) H_2SO_4 and (d) NaF concentration., Table S1: Lattice
482 parameters of the WO_3 NFs samples.

Author Contributions: Conceptualization, P.M.; investigation, A.P., M.R., A.Z.-M., J.L., P.M.; supervision, J.L, A.Z.-M. and P.M.; writing (review and editing) A.P., A.Z.-M., J.L., P.M.

Conflicts of Interest: The authors declare no conflict of interest.

References

1. who.int Available online: https://www.who.int/gho/phe/outdoor_air_pollution/burden/en/ (accessed on Jul 16, 2020).
2. Ghime, D.; Ghosh, P. Advanced Oxidation Processes: A Powerful Treatment Option for the Removal of Recalcitrant Organic Compounds. *Adv. Oxid. Process. - Appl. Trends, Prospect.* **2020**, 1–12, doi:10.5772/intechopen.90192.
3. Dewil, R.; Mantzavinos, D.; Poulios, I.; Rodrigo, M.A. New perspectives for Advanced Oxidation Processes. *J. Environ. Manage.* **2017**, *195*, 93–99, doi:10.1016/j.jenvman.2017.04.010.
4. Miklos, D.B.; Remy, C.; Jekel, M.; Linden, K.G.; Drewes, J.E.; Hübner, U. Evaluation of advanced oxidation processes for water and wastewater treatment – A critical review. *Water Res.* **2018**, *139*, 118–131, doi:10.1016/j.watres.2018.03.042.
5. Hoffmann, M.R.; Martin, S.T.; Choi, W.; Bahnemannt, D.W. Environmental Applications of Semiconductor Photocatalysis. *Chem. Rev.* **1995**, 69–96, doi:doi.org/10.1021/cr00033a004.
6. Maira, A.J.; Yeung, K.L.; Soria, J.; Coronado, J.M.; Belver, C.; Lee, C.Y.; Augugliaro, V. Gas-phase photo-oxidation of toluene using nanometer-size TiO_2 catalysts. *Appl. Catal. B Environ.* **2001**, *29*, 327–336, doi:10.1016/S0926-3373(00)00211-3.
7. Weon, S.; He, F.; Choi, W. Status and challenges in photocatalytic nanotechnology for cleaning air polluted with volatile organic compounds: Visible light utilization and catalyst deactivation. *Environ. Sci. Nano* **2019**, *6*, 3185–3214, doi:10.1039/c9en00891h.
8. Venkata Laxma Reddy, P.; Kim, K.H.; Kim, Y.H. A review of photocatalytic treatment for various air pollutants. *Asian J. Atmos. Environ.* **2011**, *5*, 181–188, doi:10.5572/ajae.2011.5.3.181.
9. Chen, X.; Mao, S.S. Titanium dioxide nanomaterials: Synthesis, properties, modifications and applications. *Chem. Rev.* **2007**, *107*, 2891–2959, doi:10.1021/cr0500535.
10. Kubacka, A.; Fernández-García, M.; Colón, G. Advanced nanoarchitectures for solar photocatalytic applications. *Chem. Rev.* **2012**, *112*, 1555–1614, doi:10.1021/cr100454n.
11. Nah, Y.C.; Paramasivam, I.; Schmuki, P. Doped TiO_2 and TiO_2 nanotubes: Synthesis and applications. *ChemPhysChem* **2010**, *11*, 2698–2713, doi:10.1002/cphc.201000276.
12. Wang, Y.; Cheng, H.; Hao, Y.; Ma, J.; Li, W.; Cai, S. Photoelectrochemical properties of metal-ion-doped TiO_2 nanocrystalline electrodes. *Thin Solid Films* **1999**, *349*, 120–125, doi:10.1016/S0040-6090(99)00239-4.
13. Guo, Y.; Quan, X.; Lu, N.; Zhao, H.; Chen, S. High photocatalytic capability of self-assembled nanoporous WO_3 with preferential orientation of (002) planes. *Environ. Sci. Technol.* **2007**, *41*, 4422–4427, doi:10.1021/es062546c.
14. Bamwenda, G.R.; Arakawa, H. Visible light induced photocatalytic activity of tungsten trioxide powders. *Appl. Catal. A Gen.* **2001**, *210*, 181–191, doi:10.1016/S0926-860X(00)00796-1.
15. Gondal, M.A.; Dastageer, M.A.; Khalil, A. Synthesis of nano-WO_3 and its catalytic activity for enhanced antimicrobial process for water purification using laser induced photo-catalysis. *Catal. Commun.* **2009**, *11*, 214–219, doi:10.1016/j.catcom.2009.10.011.
16. Waldner, G.; Brüger, A.; Gaikwad, N.S.; Neumann-Spallart, M. WO_3 thin films for photoelectrochemical purification of water. *Chemosphere* **2007**, *67*, 779–784, doi:10.1016/j.chemosphere.2006.10.024.
17. Su, X.; Li, Y.; Jian, J.; Wang, J. In situ etching WO_3 nanoplates: Hydrothermal synthesis,

photoluminescence and gas sensor properties. *Mater. Res. Bull.* **2010**, *45*, 1960–1963, doi:10.1016/j.materresbull.2010.08.011.

18. An, S.; Park, S.; Ko, H.; Lee, C. Fabrication of WO_3 nanotube sensors and their gas sensing properties. *Ceram. Int.* **2014**, *40*, 1423–1429, doi:10.1016/J.CERAMINT.2013.07.025.
19. Li, Z.; Li, J.; Song, L.; Gong, H.; Niu, Q. Ionic liquid-assisted synthesis of WO_3 particles with enhanced gas sensing properties. *J. Mater. Chem. A* **2013**, *1*, 15377, doi:10.1039/c3ta13500d.
20. Miseki, Y.; Kusama, H.; Sugihara, H.; Sayama, K. Cs-modified WO_3 photocatalyst showing efficient solar energy conversion for O_2 production and Fe (III) ion reduction under visible light. *J. Phys. Chem. Lett.* **2010**, *1*, 1196–1200, doi:10.1021/jz100233w.
21. Miseki, Y.; Kusama, H.; Sayama, K. Photocatalytic energy storage over surface-modified WO_3 using V^{5+}/V^{4+} redox mediator. *Chem. Lett.* **2012**, *41*, 1489–1491, doi:10.1246/cl.2012.1489.
22. Choi, Y.G.; Sakai, G.; Shimanoe, K.; Teraoka, Y.; Miura, N.; Yamazoe, N. Preparation of size and habit-controlled nano crystallites of tungsten oxide. *Sensors Actuators, B Chem.* **2003**, *93*, 486–494, doi:10.1016/S0925-4005(03)00195-3.
23. Santato, C.; Odziemkowski, M.; Ulmann, M.; Augustynski, J. Crystallographically oriented mesoporous WO_3 films: Synthesis, characterization, and applications. *J. Am. Chem. Soc.* **2001**, *123*, 10639–10649, doi:10.1021/ja011315x.
24. Badilescu, S.; Ashrit, P. V. Study of sol-gel prepared nanostructured WO_3 thin films and composites for electrochromic applications. *Solid State Ionics* **2003**, *158*, 187–197, doi:10.1016/S0167-2738(02)00764-6.
25. Yu, Z.; Jia, X.; Du, J.; Zhang, J. Electrochromic WO_3 films prepared by a new electrodeposition method. *Sol. Energy Mater. Sol. Cells* **2000**, *64*.
26. Brescacin, E.; Basato, M.; Tondello, E. Amorphous WO_3 films via chemical vapor deposition from metallorganic precursors containing phosphorus dopant. *Chem. Mater.* **1999**, *11*, 314–323, doi:10.1021/cm980741n.
27. Palgrave, R.G.; Parkin, I.P. Aerosol assisted chemical vapour deposition of photochromic tungsten oxide and doped tungsten oxide thin films. *J. Mater. Chem.* **2004**, *14*, 2864–2867, doi:10.1039/b406337f.
28. Tsuchiya, H.; Macak, J.M.; Sieber, I.; Taveira, L.; Ghicov, A.; Sirotna, K.; Schmuki, P. Self-organized porous WO_3 formed in NaF electrolytes. *Electrochem. commun.* **2005**, *7*, 295–298, doi:10.1016/j.elecom.2005.01.003.
29. Ng, C.; Ye, C.; Ng, Y.H.; Amal, R. Flower-shaped tungsten oxide with inorganic fullerene-like structure: Synthesis and characterization. *Cryst. Growth Des.* **2010**, *10*, 3794–3801, doi:10.1021/cg100625m.
30. Srichaiyaperk, T.; Aiempanakit, K.; Horprathum, M.; Eiamchai, P.; Chananonnawathorn, C.; Limwichean, S.; Chindaudom, P. Effects of annealing treatment on WO_3 thin films prepared by DC reactive magnetron sputtering. *Adv. Mater. Res.* **2014**, *979*, 248–250, doi:10.4028/www.scientific.net/AMR.979.248.
31. Liang, Y.C.; Chang, C.W. Preparation of orthorhombic WO3 thin films and their crystal quality-dependent dye photodegradation ability. *Coatings* **2019**, *9*, doi:10.3390/COATINGS9020090.
32. Marszalek, K. Magnetron-sputtered WO_3 films for electrochromic devices. *Thin Solid Films* **1989**, *175*, 227–233, doi:10.1016/0040-6090(89)90832-8.
33. M., B.B.; K., V.M. Structural, morphological and optical properties of electron beam evaporated WO_3 thin films . *J. Taibah Univ. Sci.* **2017**, *11*, 1232–1237, doi:10.1016/j.jtusci.2016.12.003.
34. Sivakumar, R.; Gopalakrishnan, R.; Jayachandran, M.; Sanjeeviraja, C. Preparation and characterization of electron beam evaporated WO_3 thin films. *Opt. Mater. (Amst).* **2007**, *29*, 679–687,

doi:10.1016/j.optmat.2005.11.017.

35. Malm, J.; Sajavaara, T.; Karppinen, M. Atomic layer deposition of WO_3 thin films using $W(CO)_6$ and O_3 precursors. *Chem. Vap. Depos.* **2012**, *18*, 245–248, doi:10.1002/cvde.201206986.
36. Li, B.; Gao, X.; Zhang, H.C.; Yuan, C. Energy modeling of electrochemical anodization process of titanium dioxide nanotubes. *ACS Sustain. Chem. Eng.* **2014**, *2*, 404–410, doi:10.1021/sc400304h.
37. Berger, S.; Tsuchiya, H.; Ghicov, A.; Schmuki, P. High photocurrent conversion efficiency in self-organized porous WO_3. *Appl. Phys. Lett.* **2006**, *88*, 88–91, doi:10.1063/1.2206696.
38. Caramori, S.; Cristino, V.; Meda, L.; Tacca, A.; Argazzi, R.; Bignozzi, C.A. Efficient anodically grown WO_3 for photoelectrochemical water splitting. *Energy Procedia* **2012**, *22*, 127–136, doi:10.1016/j.egypro.2012.05.214.
39. Nah, Y.C.; Ghicov, A.; Kim, D.; Schmuki, P. Enhanced electrochromic properties of self-organized nanoporous WO_3. *Electrochem. commun.* **2008**, *10*, 1777–1780, doi:10.1016/j.elecom.2008.09.017.
40. Ou, J.Z.; Rani, R.A.; Balendhran, S.; Zoolfakar, A.S.; Field, M.R.; Zhuiykov, S.; O'Mullane, A.P.; Kalantar-Zadeh, K. Anodic formation of a thick three-dimensional nanoporous WO_3 film and its photocatalytic property. *Electrochem. commun.* **2013**, *27*, 128–132, doi:10.1016/j.elecom.2012.11.009.
41. Ou, J.Z.; Balendhran, S.; Field, M.R.; McCulloch, D.G.; Zoolfakar, A.S.; Rani, R.A.; Zhuiykov, S.; O'Mullane, A.P.; Kalantar-Zadeh, K. The anodized crystalline WO_3 nanoporous network with enhanced electrochromic properties. *Nanoscale* **2012**, *4*, 5980–5988, doi:10.1039/c2nr31203d.
42. Mukherjee, N.; Paulose, M.; Varghese, O.K.; Mor, G.K.; Grimes, C.A. Fabrication of nanoporous tungsten oxide by galvanostatic anodization. *J. Mater. Res.* **2003**, *18*, 2296–2299, doi:10.1557/JMR.2003.0321.
43. Yu, L.; Kalantar-zadeh, K.; Zhu, J.; Latham, K.; Wlodarski, W.; Hu, Z.; Sadek, A.Z.; Breedon, M.; Zheng, H.; Bhargava, S.K.; et al. High-Temperature Anodized WO_3 Nanoplatelet Films for Photosensitive Devices . *Langmuir* **2009**, *25*, 9545–9551, doi:10.1021/la901944x.
44. Ng, C.; Ng, Y.H.; Iwase, A.; Amal, R. Influence of annealing temperature of WO_3 in photoelectrochemical conversion and energy storage for water splitting. *ACS Appl. Mater. Interfaces* **2013**, *5*, 5269–5275, doi:10.1021/am401112q.
45. Nischk, M.; Mazierski, P.; Gazda, M.; Zaleska, A. Ordered TiO_2 nanotubes: The effect of preparation parameters on the photocatalytic activity in air purification process. *Appl. Catal. B Environ.* **2014**, *144*, 674–685, doi:10.1016/j.apcatb.2013.07.041.
46. Macak, J.M.; Schmuki, P. Anodic growth of self-organized anodic TiO_2 nanotubes in viscous electrolytes. *Electrochim. Acta* **2006**, *52*, 1258–1264, doi:10.1016/j.electacta.2006.07.021.
47. Pourbaix, M. Atlas of electrochemical equilibria in aqueous solutions 2 English ed. *Natl. Assoc. Corros. Eng. Houston, TX,* **1974**, doi:10.1016/0022-0728(67)80059-7.
48. Roy, P.; Berger, S.; Schmuki, P. TiO_2 nanotubes: Synthesis and applications. *Angew. Chemie - Int. Ed.* **2011**, *50*, 2904–2939, doi:10.1002/anie.201001374.
49. Macak, J.M.; Tsuchiya, H.; Ghicov, A.; Yasuda, K.; Hahn, R.; Bauer, S.; Schmuki, P. TiO_2 nanotubes: Self-organized electrochemical formation, properties and applications. *Curr. Opin. Solid State Mater. Sci.* **2007**, *11*, 3–18, doi:10.1016/J.COSSMS.2007.08.004.
50. Chai, Y.; Tam, C.W.; Beh, K.P.; Yam, F.K.; Hassan, Z. Porous WO_3 formed by anodization in oxalic acid. *J. Porous Mater.* **2013**, *20*, 997–1002, doi:10.1007/s10934-013-9675-5.
51. Anik, M.; Osseo-Asare, K. Effect of pH on the Anodic Behavior of Tungsten. *J. Electrochem. Soc.* **2002**, *149*, B224, doi:10.1149/1.1471544.
52. Macdonald, D.D.; Sikora, E.; Sikora, J. The kinetics of growth of the passive film on tungsten in acidic

phosphate solutions. *Electrochim. Acta* **1998**, *43*, 2851–2861, doi:10.1016/S0013-4686(98)00026-7.

53. Lai, C.W. Photocatalysis and photoelectrochemical properties of tungsten trioxide nanostructured films. *Sci. World J.* **2014**, *2014*, doi:10.1155/2014/843587.

54. El-Basiouny, M.S.; Hassan, S.A.; Hefny, M.M. On the electrochemical behaviour of tungsten: the formation and dissolution of tungsten oxide in sulphuric acid solutions. *Corros. Sci.* **1980**, *20*, 909–917, doi:10.1016/0010-938X(80)90123-7.

55. Baserga, A.; Russo, V.; Di Fonzo, F.; Bailini, A.; Cattaneo, D.; Casari, C.S.; Li Bassi, A.; Bottani, C.E. Nanostructured tungsten oxide with controlled properties: Synthesis and Raman characterization. *Thin Solid Films* **2007**, *515*, 6465–6469, doi:10.1016/j.tsf.2006.11.067.

56. Daniel, M.F.; Desbat, B.; Lassegues, J.C.; Gerand, B.; Figlarz, M. Infrared and Raman study of WO_3 tungsten trioxides and WO_3xH_2O tungsten trioxide tydrates. *J. Solid State Chem.* **1987**, *67*, 235–247, doi:10.1016/0022-4596(87)90359-8.

57. Butler, M.A. Photoelectrolysis and physical properties of the semiconducting electrode WO_2. *J. Appl. Phys.* **1977**, *48*, 1914–1920, doi:10.1063/1.323948.

58. Teoh, L.G.; Shieh, J.; Lai, W.H.; Hung, I.M.; Hon, M.H. Structure and optical properties of mesoporous tungsten oxide. *J. Alloys Compd.* **2005**, *396*, 251–254, doi:10.1016/j.jallcom.2004.12.005.

59. Fujihara, S.; Ogawa, Y.; Kasai, A. Tunable visible photoluminescence from ZnO thin films through Mg-doping and annealing. *Chem. Mater.* **2004**, *16*, 2965–2968, doi:10.1021/cm049599i.

60. Sreekantan, S.; Saharudin, K.A.; Lockman, Z.; Tzu, T.W. Fast-rate formation of TiO_2 nanotube arrays in an organic bath and their applications in photocatalysis. *Nanotechnology* **2010**, *21*, doi:10.1088/0957-4484/21/36/365603.

61. Liang, Y.; Lin, S.; Liu, L.; Hu, J.; Cui, W. Oil-in-water self-assembled Ag@AgCl QDs sensitized Bi_2WO_6: Enhanced photocatalytic degradation under visible light irradiation. *Appl. Catal. B Environ.* **2015**, *164*, 192–203, doi:10.1016/j.apcatb.2014.08.048.

62. Zhu, Z.; Yan, Y.; Li, J. Preparation of flower-like BiOBr-WO_3-Bi_2WO_6 ternary hybrid with enhanced visible-light photocatalytic activity. *J. Alloys Compd.* **2015**, *651*, 184–192, doi:10.1016/j.jallcom.2015.08.137.

63. Kalantar-zadeh, K.; Sadek, A.Z.; Zheng, H.; Bansal, V.; Bhargava, S.K.; Wlodarski, W.; Zhu, J.; Yu, L.; Hu, Z. Nanostructured WO_3 films using high temperature anodization. *Sensors Actuators, B Chem.* **2009**, *142*, 230–235, doi:10.1016/j.snb.2009.08.014.

64. Zhuang, H.; Lin, C.; Lai, Y.; Sun, L.; Li, J. Some Critical Structure Factors of Titanium Oxide Nanotube Array in Its Photocatalytic Activity Some Critical Structure Factors of Titanium Oxide Nanotube Array in Its Photocatalytic Activity. **2007**, 4735–4740, doi:10.1021/es0702723.